Nuclear Instruments and Methods in Physics Research A 845 (2017) 579–582

Contents lists available at ScienceDirect

Nuclear Instruments and Methods in Physics Research A

journal homepage: www.elsevier.com/locate/nima

# Annihilation detector for an in-beam spectroscopy apparatus to measure the ground state hyperfine splitting of antihydrogen

Clemens Sauerzopf [a,*], Aaron A. Capon [a], Martin Diermaier [a], Markus Fleck [a], Bernadette Kolbinger [a], Chloé Malbrunot [a,b], Oswald Massiczek [a], Martin C. Simon [a], Stefan Vamosi [a], Johann Zmeskal [a], Eberhard Widmann [a]

[a] Stefan Meyer Institute for subatomic Physics, Austrian Academy of Sciences, Boltzmanngasse 3, 1090 Wien, Austria
[b] Organisation Européenne pour la Recherche Nucléaire (CERN), 1211 Geneva 23, Switzerland

ARTICLE INFO

*Article history:*
Received 15 March 2016
Received in revised form
6 June 2016
Accepted 6 June 2016
Available online 8 June 2016

*Keywords:*
Antihydrogen
Scintillator
Hodoscope
Silicon photomultiplier

ABSTRACT

The matter-antimatter asymmetry observed in the universe today still lacks a quantitative explanation. One possible mechanism that could contribute to the observed imbalance is a violation of the combined Charge-, Parity- and Time symmetries (CPT). A test of CPT symmetry using anti-atoms is being carried out by the ASACUSA-CUSP collaboration at the CERN Antiproton Decelerator using a low temperature beam of antihydrogen—the most simple atomic system built only of antiparticles. While hydrogen is the most abundant element in the universe, antihydrogen is produced in very small quantities in a laboratory framework. A detector for in-beam measurements of the ground state hyperfine structure of antihydrogen has to be able to detect very low signal rates within high background. To fulfil this challenging task, a two layer barrel hodoscope detector was developed. It is built of plastic scintillators with double sided readout via Silicon Photomultipliers (SiPMs). The SiPM readout is done using novel, compact and cost efficient electronics that incorporate power supply, amplifier and discriminator on a single board. This contribution will evaluate the performance of the new hodoscope detector.



## 1. Introduction

For the production of antihydrogen, low energetic antiprotons are extracted from the CERN Antiproton Decelerator (AD) facility, and are collected by a first Penning trap (MUSASHI trap). In a process called “mixing”, the trapped antiprotons are then combined with positrons inside a so-called CUSP trap which is a combination of electrostatic fields and inhomogeneous magnetic fields created by a pair of anti Helmholtz coils [1]. The produced neutral antihydrogen atoms can escape the trapping field, and are then focused, through the spectroscopy apparatus [2], towards the detector by strong cusp field gradientsčitecusp1.

The amount of antihydrogen produced by this techniques is low, and even less is reaching the end of the spectroscopy apparatus, imposing unique challenges for the design and operation of the detector. These challenges include the detection of very rare annihilation events under tough background conditions, especially, since the detector needs good discrimination probabilities between cosmic rays, annihilations in the beampipe, and the antihydrogen annihilations in the detector. Additionally, the detector is required to perform equally well for beam diagnosis and for the measurement of the ground state hyperfine transitions in antihydrogen.

## 2. Detector

The ASACUSA antihydrogen detector consists of a central detector and a surrounding two layer hodoscope. The central detector unit is a 10 cm diameter bismuth germanate (BGO) disc with a thickness of 5 mm. The BGO crystal is read by 4 Hamamatsu H8500 multi anode photomultipliers featuring $8 \times 8$ pixels each [3].

Each layer of the hodoscope is composed of 32 plastic scintillator bars (material EJ-200). In the case of the inner layer, the individual bars are 300 mm long with a cross section of $20 \times 5$ mm$^2$. The bars of the outer layer have a length of 450 mm and a cross section of $35 \times 5$ mm$^2$. Light guides are glued to the scintillator bars on both sides, reducing the cross section down to $8 \times 5$ mm$^2$ over a distance of 40 mm for the inner hodoscope layer and 75 mm in the case of the outer hodoscope bars. Two KETEK SiPMs,

* Corresponding author.
*E-mail address:* clemens.sauerzopf@oeaw.ac.at (C. Sauerzopf).

http://dx.doi.org/10.1016/j.nima.2016.06.023

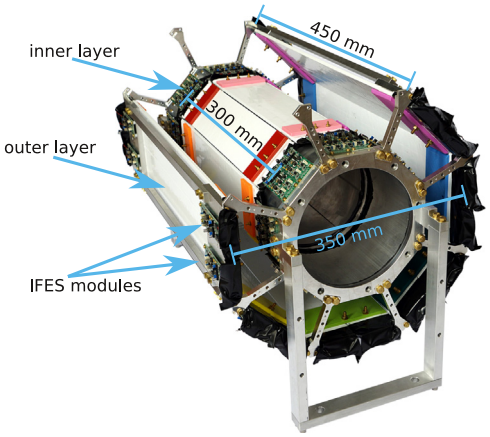


**Fig. 1.** Photograph of the ASACUSA hodoscope detector. Two outer panels, along with all cables, have been removed for better visibility. The IFES modules for SiPM readout are mounted.

connected in series, of type PM3350TS ($3 \times 3$ mm$^2$ surface, 50 µm micropixel size, with optical trench separation) are glued on each side of every detector bar. This results in 128 readout channels with 256 SiPMs for the full hodoscope. The SiPMs are read by self developed frontend modules called IFES [4]. The IFES modules provide the diode bias, a discriminator signal, an analogue differential output signal, and a differential SiPM readout. The amplified analogue signal is recorded by five CAEN V1742 waveform digitisers, whereas, the discriminator signal is used to produce the data acquisition trigger. The hodoscope is displayed in Fig. 1 with the cabling removed, and the IFES modules mounted.

Each individual bar is wrapped using aluminium foil. In the case of the outer hodoscope layer, two bars are wrapped together in light-blocking foil to ensure light tightness. Two of the scintillator packs are then mounted onto a colour coded removable panel for installation on the detector frame. In the case of the inner layer, four bars are combined and wrapped in the light blocking foil. The bars of the inner layer are mounted onto a 1 mm thick stainless steel pipe that stabilises the detector frame. The system has a total length of 606 mm, and a diameter of 350 mm for the outer hodoscope layer and a diameter of 200 mm for the inner layer.

## 3. Performance evaluation

The detector characterisation presented here uses cosmic rays and includes both tests of the individual components, and performance evaluation of the fully assembled structure with the complete data acquisition in place.

### 3.1. Time-of-flight, and position resolution

In a laboratory frame the individual detector components were characterised and tested using cosmic rays. Measurements for inferring the time-of-flight (ToF) resolution have been performed by placing two hodoscope bars, wrapped in aluminium foil, on top of each other in a light tight box. The SiPMs were operated using the IFES modules, and the data was recorded using a CAEN DT5742 digitiser with 5 GS/s Fig. 2A. The data were analysed using a self developed modular waveform analysis library [5]. The position resolution was measured by placing a small plastic scintillator with a thickness of 1 mm, a width of 3 mm, and a length of 27 mm perpendicular to the hodoscope bars on both sides Fig. 2B. For the inner bar, the distance from the centre of the bar was 123.5 mm, and for the outer hodoscope the distance was 199.5 mm.

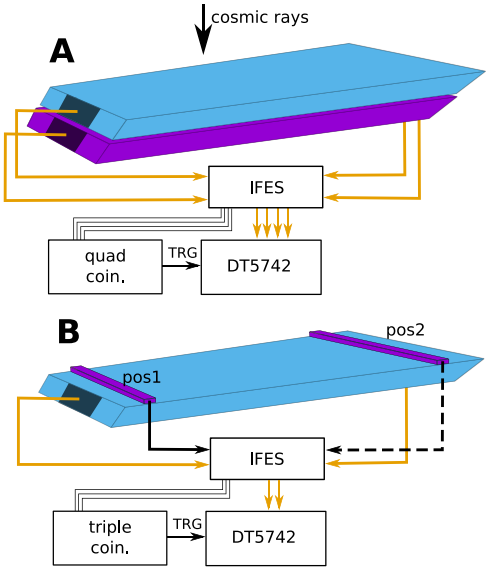


**Fig. 2.** Schematic diagrams of laboratory measurements. A: setup for ToF measurements. Two identical hodoscope bars are placed on top of each other. A readout trigger for the DT5742 is generated by a quad coincidence between SiPM signals from both sides of each bar. B: Setup for position resolution measurements. A triple coincidence between a small reference scintillator and both sides of the hodoscope bar is used to generate a readout trigger for the waveform digitiser.

In the case of the ToF measurement a coincidence between both scintillator bars was used as trigger condition. Whereas, the position resolution was measured by requiring a coincidence between the hodoscope bar and the small plastic scintillator.

In Fig. 3 the ToF performances for both hodoscope layers are shown. The ToF spectra were obtained by using constant fraction (CF) timestamps of both sides of each scintillator, and then calculating the mean time difference between the two bars. The timing resolution is then inferred by performing an orthogonal distance regression (ODR) [6] with a Gaussian distribution.

The ToF resolution between two bars of the outer hodoscope was measured to be **551 ± 5 ps** full width half maximum (FWHM). In the case of the inner detector bars, the ToF resolution is **497 ± 3 ps** FWHM.

A relativistic particle with a velocity close to the speed of light can only travel a distance of ≈ 30 cm in 1 ns. It follows that the achieved ToF resolution allows one to impose stringent cuts for

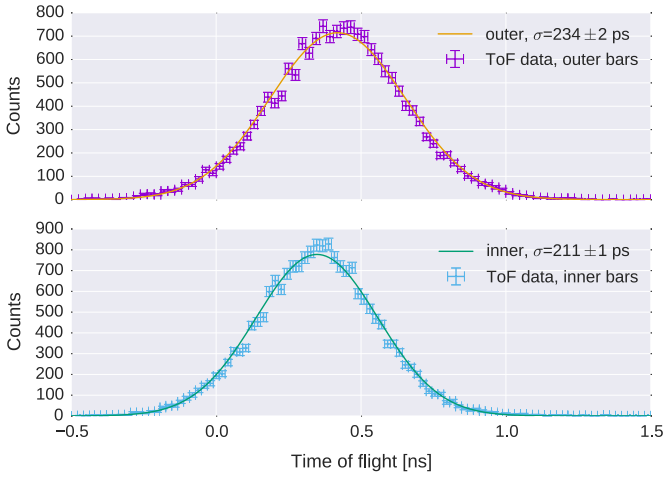


**Fig. 3.** ToF measurements for inner and outer hodoscope bars. Top graph: measured mean time difference between two outer hodoscope bars, with Gaussian ODR. Bottom: measured mean time difference between two inner hodoscope bars, with Gaussian ODR.

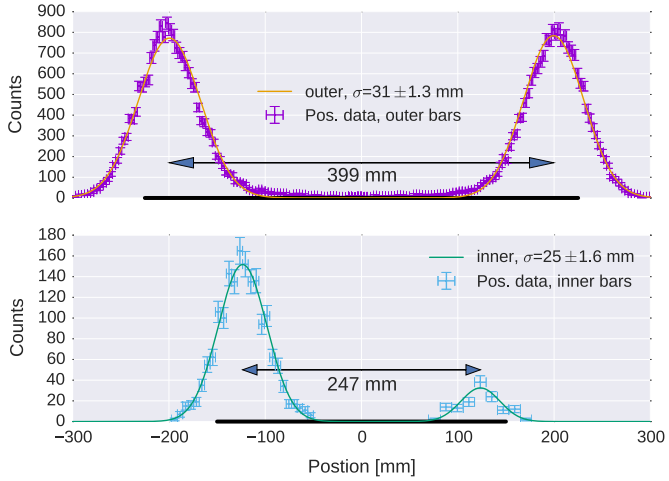


**Fig. 4.** Measurements for determining the position resolution for both hodoscope bars. The two peaks correspond to the positions of a reference scintillator, indicated by the arrow. The length of the hodoscope bar is represented by the black line on the abscissa. Top: position resolution for the outer hodoscope bars with Gaussian ODR. Bottom: position resolution for the inner hodoscope bars with Gaussian ODR. The asymmetry between the two peaks for the inner hodoscope arises from the reduced measurement time for the second peak.

separating events that are generated inside of the detector, due to antihydrogen annihilations, from those background particles passing through with a distant origin.

Evaluating the position resolution along the bar was attempted with both amplitude information and timing differences. Due to the high light output and the resulting saturation of the SiPMs, the amplitude evaluation was demonstrated to be unfeasible. Whereas, utilising the difference between the CF timestamps of both side of the bars yielded satisfactory results.

The position resolution was measured by fitting the CF time differences ($\Delta t$) between both sides of one hodoscope bar with a normal distribution. The two resulting Gaussian location parameters in the time domain ($\mu_1$ and $\mu_2$) are used to calculate a scale factor ($f$) and offset ($T$) with the spacial distance of the two measurements ($l$), for transforming the time difference into a position ($x$) along the bar

$$f = \frac{l}{\mu_2 - \mu_1}; \quad T = \frac{\mu_1 + \mu_2}{2}; \quad x = (\Delta t - T)f. \tag{1}$$

The resulting distributions, after reconstructing the hit positions using Eq. (1), are shown in Fig. 4. The two positions of the reference scintillator correspond to the central moments of the two Gaussian shaped peaks in each spectrum.

Measurement for inferring the position resolution are very time consuming due to the small cross section of the reference detector. From the evaluation of the data for the outer hodoscope it was concluded, that less data for the required precision in the inner hodoscope is required.

From the ODR one can extract the position resolution. In the case of the outer hodoscope bar the resolution was determined to be $\mathbf{73 \pm 3\ mm}$ FWHM ($16.2 \pm 0.7\%$ of bar length). For the inner hodoscope layer, the resolution becomes $\mathbf{59 \pm 3.8\ mm}$ FWHM ($19 \pm 1.3\%$ of bar length). This result enables the implementation of rudimentary 3D tracking.

### 3.2. Multiplicity, and angular distributions

An evaluation of the detector performance for the full assembly was done by measuring cosmic rays. All data were recorded with CAEN V1742 waveform digitisers (5 GS/s), and were analysed by the waveform library [5]. The final analysis was done using the rootpy [7] and scipy [8] packages. Simulations were performed with the Geant4 toolkit [9], and the CRY library [10] using a $3 \times 3\ m^2$ particle emitting surface placed 30 cm above the detector geometry. The statistical significance of deviations between data and simulations, and between data of inner and outer hodoscope layer is evaluated using Pearson's $\chi^2$ test. All reported $p$ values were calculated under the null hypothesis that there is significant deviation between simulations and measured data.

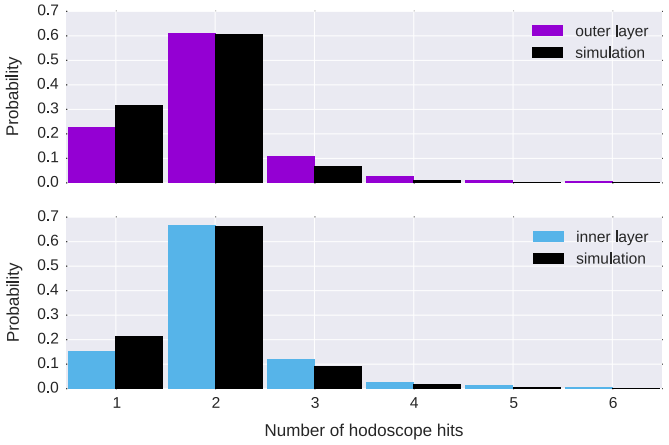


**Fig. 5.** Detector multiplicity measurement with cosmic rays. Top: inner hodoscope layer with simulation. $p=0.999$. Bottom: outer hodoscope layer with simulation. $p=0.995$. Between inner and outer hodoscope layer the data agree with $p=0.998$. The data are normalised as probabilities.

A comparison between simulations and measured multiplicity distribution is shown in Fig. 5. The agreement between the predictions and the measurements is significant with all $p$ values being $> 0.99$. Small deviations are observed that can be attributed to inaccuracies and computational limitations of the simulation conditions.

In Fig. 6, the angular distribution, represented by the hodoscope bar number, for cosmic data is shown. In the top panel the distributions for both hodoscope layers are compared. In the other panels, the measured data are compared with Geant4 and CRY simulations. All measurements are in good agreement with simulations and agree with each other with all $p$ values being $> 0.99$.

From the results presented in Figs. 5 and 6 one can conclude, that the hodoscope of the ASACUSA antihydrogen detector is well

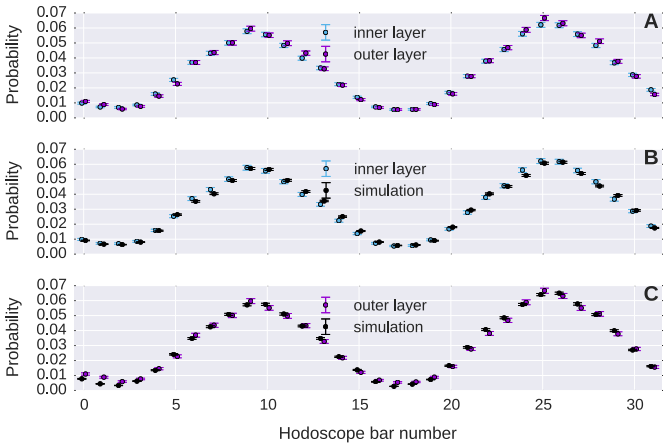


**Fig. 6.** Angular distribution of cosmic rays as recorded with the hodoscope detector. The bar numbers 0 to 31 cover 360°. A: Comparison of data for the inner and the outer hodoscope. $p=0.998$. B: Comparison of inner hodoscope data with simulations. $p=0.999$. C: Comparison of outer hodoscope data with simulations. The data are normalised as probabilities. $p=0.992$.

prepared for measuring antihydrogen annihilations. The results show that the detector can discriminate these rare events against a high level of background from cosmic rays, and annihilations of stray antihydrogen atoms on the beampipe walls.

## 4. Summary

A two layer hodoscope detector, made of plastic scintillators and read out by SiPMs, was developed and successfully tested. In a test run with cosmic rays, the full detector performed as required for background discrimination, and the data reproduced the expected distributions from Geant4 simulations with the CRY library.

Individual detector components have been further examined in a laboratory experiment to determine the position resolution along the bar axis, allowing rudimentary 3D tracking for a future analysis. Furthermore, the ToF resolution between two hodoscope bars was measured. In particular, the ToF resolution between two antipodal outer bars was found to be **551** $\pm$ **5 ps** FWHM, therefore directly allowing discrimination between particles penetrating the detector from the outside and particles originating from annihilation events in the centre.

## Acknowledgements

This work was funded by the European Research Council under European Union's Seventh Framework Programme (FP7/2007–2013)/ERC Grant Agreement (291242) and the Austrian Ministry of Science and Research, Austrian Science Fund (FWF): DK PI (W 1252). Hardware development and manufacturing was performed by the SMI workshop.

## References

[1] Y. Enomoto, et al., Synthesis of cold antihydrogen in a cusp trap, Phys. Rev. Lett. 105 (2010) 243401, http://dx.doi.org/10.1103/PhysRevLett.105.243401.
[2] C. Malbrunot, et al., Spectroscopy apparatus for the measurement of the hyperfine structure of antihydrogen, Hyperfine Interact. 228 (1) (2014) 61–66, http://dx.doi.org/10.1007/s10751-014-1013-z.
[3] Y. Nagata, et al., The development of the antihydrogen beam detector and the detection of the antihydrogen atoms for in-flight hyperfine spectroscopy, Journal of Physics: Conference Series 635 (2) (2015) 022061 http://stacks.iop.org/1742-6596/635/i=2/a=022061.
[4] C. Sauerzopf, et al., Intelligent front-end electronics for silicon photodetectors (IFES), Nucl. Instrum. Methods Phys. Res. Sect. A ⟨http://dx.doi.org/10.1016/j.nima.2016.02.098⟩ URL ⟨http://www.sciencedirect.com/science/article/pii/S0168900216300158⟩.
[5] C. Sauerzopf, Waveformlibrary v1.0.0, Dec. 2015. ⟨http://dx.doi.org/10.5281/zenodo.35341⟩.
[6] P.T. Boggs, J.E. Rogers, Orthogonal distance regression, in: P.J. Brown, W.A. Fuller (Eds.), Statistical Analysis of Measurement Error Models and Applications: Proceedings of the AMS-IMS-SIAM Joint Summer Research Conference Held June 10–16, 1989, with Support from the National Science Foundation and the US Army Research Office, Vol. 112, American Mathematical Soc., 1990, p. 183.
[7] N. Dawe, et al., rootpy: 0.8.0 Jun. 2015, ⟨http://dx.doi.org/10.5281/zenodo.18897⟩.
[8] S. van der Walt, S.C. Colbert, G. Varoquaux, The numpy array: A struc191ture for efficient numerical computation, Comput. Sci. Eng. 13 (2) (2011) 22–30, http://dx.doi.org/10.1109/MCSE.2011.37.
[9] S. Agostinelli, et al., Geant4–a simulation toolkit, Nucl. Instrum. Methods Phys. Res. Sect. A 506 (3) (2003) 250–303, http://dx.doi.org/10.1016/S0168-9002(03)01368-8.
[10] C. Hagmann, D. Lange, D. Wright, Cosmic-ray shower generator (cry) for monte carlo transport codes, in: Proceedings of IEEE Nuclear Science Symposium Conference Record, 2007. NSS'07, vol. 2, Honolulu, Hawaii, USA, 2007, pp. 1143–1146, ⟨http://dx.doi.org/10.1109/NSSMIC.2007.4437209⟩.